Mechanism of the High-T_c Superconducting Dynamo: Models and Experiment

Ratu Mataira,[1,*] Mark Ainslie,[2] Andres Pantoja,[1] Rod Badcock,[1] and Chris Bumby[1,†]

[1] *Robinson Research Institute, Faculty of Engineering, Victoria University of Wellington, 69 Gracefield Road, Lower Hutt 5010, New Zealand*

[2] *Department of Engineering, University of Cambridge, Trumpington Street, Cambridge CB2 1PZ, United Kingdom*

(Received 5 April 2020; accepted 12 June 2020; published 6 August 2020)

High-T_c superconducting (HTS) dynamos are experimentally proven devices that can produce large (more than a kiloamp) dc currents in superconducting circuits, without the thermal leak associated with copper current leads. However, these dc currents are theoretically controversial, as it is not immediately apparent why a device that is topologically identical to an ac alternator should give a dc output at all. Here, we present a finite-element model and a comparison of it with experiment that fully explain this effect. It is shown that the dc output arises naturally from Maxwell's laws when time-varying overcritical eddy currents are induced to circulate in a HTS sheet. We first show that our finite-element model replicates all of the experimental electrical behavior reported so far for these devices, including the dc output characteristics and transient electrical waveforms. Direct experimental evidence for the presence of circulating eddy currents is also obtained through measurements of the transient magnetic field profile across the HTS tape, using a linear Hall array. These results are also found to agree closely with predictions from the finite-element model. Following this experimental validation, calculated sheet current densities and the associated local electric fields are examined for a range of frequencies and net transport currents. We find that the electrical output from a HTS dynamo is governed by the competition between transport and eddy currents induced as the magnet transits across the HTS tape. The eddy currents are significantly higher (approximately 1.5 times) than the local critical current density, and hence experience a highly nonlinear local resistivity. This nonlinearity breaks the symmetry observed in a normal ohmic material, which usually requires the net transport current to vary linearly with the average electric field. The interplay between local current densities and nonlinear resistivities (which both vary in time and space) is shown to systematically give rise to the key observed parameters of experimental HTS dynamo devices: the open-circuit voltage, the internal resistance, and the short-circuit current. Finally, we identify that the spatial boundaries formed by each edge of the HTS stator tape play a vital role in determining the total dc output. This offers the potential to develop alternative designs for HTS dynamo devices, in which the internal resistance is greatly reduced and the short-circuit current is substantially increased.

DOI: 10.1103/PhysRevApplied.14.024012

I. INTRODUCTION

High-T_c superconducting (HTS) dynamos [1–13] and other similar HTS "flux pumps" [14–22] have been receiving continuing attention recently, as they offer a potential solution to the dc current-injection problem in a wide range of superconducting machines [23] and magnets [24,25]. Specifically, the HTS dynamo is of interest for its predicted ability to drive a large [26,27] dc current without the associated heat leak of traditional current leads [28]. This current is provided by a near-zero source impedance, which reduces the risk of an externally initiated "driven" quench [29,30]. Such high-current low-impedance sources could enable types of coil design that avoid many of the operating risks associated with high-inductance high-voltage superconducting coils [31,32]. However, the dc output observed from experimental HTS dynamo devices [7] has presented physicists with a conundrum, as this device is topologically identical to an ac alternator described by Faraday [33] and hence should not be expected to produce a dc electromotive force (emf). This has led some authors to propose explanations based upon exotic phenomena such as quantum flux coupling [34] or flux ratcheting [21]. Such phenomena are unnecessary, as the dc

*ratu.mataira@vuw.ac.nz

†chris.bumby@vuw.ac.nz

output produced by a HTS dynamo arises naturally from Maxwell's laws [12] when applied to a situation in which eddy currents flow in a thin sheet exhibiting a highly nonlinear local resistivity. Here, we now develop the model introduced in Ref. [12] to provide a detailed explanation of how the nonlinear resistivity changes the electromagnetic physics of the HTS dynamo and hence gives rise to a dc voltage component.

Simple application of Faraday's law to a closed path, C, experiencing a periodic applied magnetic field cycle enables the time-averaged dc value of the emf to be stated as

$$\int_t^{t+P} dt \oint_C d\vec{l} \cdot \vec{E} = \Phi\big|_{t+P} - \Phi\big|_t = 0, \qquad (1)$$

where Φ is the magnetic flux enclosed by the path C, and P is the period of the cycle. However, it should be noted that the emf and the output voltage are not necessarily identical, as the emf does not include any resistive potential drops that may occur between the device terminals. In the HTS dynamo, eddy currents flow in the plane of the stator tape and experience local flux-flow resistance, which varies in both time and space over the duration of one cycle. To understand the impact of these locally circulating currents, we must therefore take care to formulate the underlying electromagnetic theory explicitly.

Finite-element (FE) modeling now enables computation of the local current density at each point within a HTS conductor experiencing a time-varying applied magnetic field. Through using the H-formulation [35–39] to solve Faraday's and Ampère's laws, a FE model of a HTS dynamo operating in the *open-circuit* condition has been produced [12]. This has been used to show that the open-circuit voltage output arises due to the presence of large overcritical eddy currents that flow in the HTS stator for a short period of each rotor cycle and act to "partially rectify" the induced emf.

Here we now extend this FE model to the *closed-circuit* case, thus enabling current and voltage outputs to be fully calculated for the full range of operating conditions of the device. We show that this simple two-dimensional (2D) model captures all of the essential electrical behavior that has been observed in experiments [3,7,40], including linear dc I-V characteristics, linear frequency dependences of both the internal resistance and the output voltage, and transient voltage waveforms. We also report further validation of the FE model through experimental measurements of the transient local magnetic field in the plane of the HTS stator tape, which confirm the presence of large overcritical circulating currents as the rotor magnet traverses the stator tape. Through interpreting results from the FE model, we find that both the short-circuit current (I_{sc}) and the apparent internal resistance (R_{int}) of the dynamo arise from competition between the net transport current I_T and the local circulating eddy currents. This understanding implies that HTS dynamo designs incorporating much wider stators should exhibit improved performance, as has been reported experimentally [9,41].

II. EXPERIMENTAL METHODS

Data are collected using an experimental HTS dynamo similar to that studied in previous work [12,40], depicted in Fig. 1(a). The dynamo stator is made from 12-mm-wide HTS coated-conductor tape (SCS12050 AP, SuperPower Inc.). The superconducting layer (1 μm thick) is deposited onto a 50-μm-thick Hastelloy substrate, which is then electroplated with 25 μm of copper stabilizer on each side of the tape. The transport critical current, I_c, of the stator tape used here is measured and found to be 293 A at 77 K (using the 1-μV criterion). A Nd-Fe-B permanent magnet 12.7 mm long, 12.7 mm deep, and 3.2 mm wide, magnetized throughout its depth, is mounted within an aluminum rotor such that the outer face of the magnet rotates with a radius of 35 mm. The stator tape is positioned perpendicular to the plane of rotation such that the vector normal to the tape surface faces in toward the rotor axis, with a flux gap g of 3.7 mm between the stator tape and the rotor circumference. The ends of the stator tape are soldered onto copper current leads that are connected to an external electronic

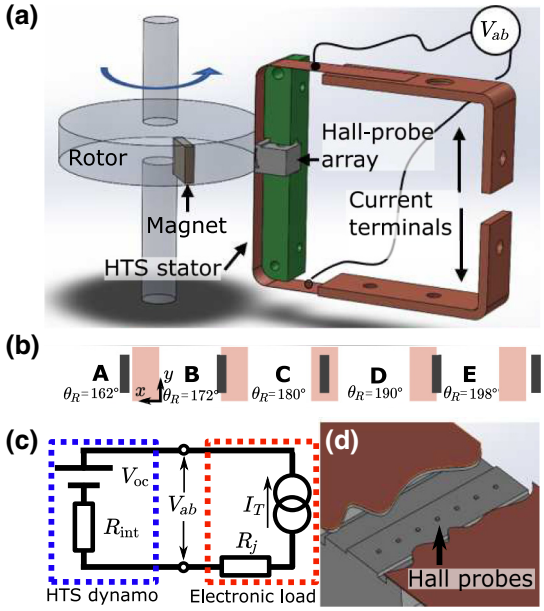

FIG. 1. (a) Schematic illustration of the HTS dynamo, including the rotor magnet, rotor housing, HTS stator, voltage leads, Hall-probe array, and current terminations. (b) Illustrated key rotor positions θ_R, as viewed from the Hall-probe array. (c) Circuit diagram showing the dynamo as a voltage V_{oc} and an internal resistance R_{int}, and the current source, current leads, termination blocks, and joints combined into a single electronic load R_j. (d) Cutaway view from the rotor side of the stator showing the Hall probes in the array.

current supply. The combination of the leads and the external current supply acts as an electronic load for the output of the HTS dynamo [5,8]; see Fig. 1(c).

Voltage taps are positioned on the stator tape such that small variations in position do not alter the measured dc output from the device [7]. However, small displacements of the voltage-tap leads will always change the inductive emf pickup of the total loop. To remove the influence of the arbitrary emf pickup from the voltage-tap leads, we make measurements with the device both at room temperature, $V_{300\,\mathrm{K}}$, and in liquid nitrogen, $V_{77\,\mathrm{K}}$, enabling differentiation between the signals obtained in the normal and superconducting states, respectively. As long as the applied magnetic field is much higher than any internal field produced by induced eddy currents in the HTS tape, $V_{300\,\mathrm{K}}$ can be considered a measurement of the emf induced by the magnet in the closed loop formed by the stator tape and the tap leads. This allows us to define the difference between the induced emf and the actual measured voltage across the stator tape as

$$\Delta V(t) = V_{77\,\mathrm{K}}(t) - V_{300\,\mathrm{K}}(t), \tag{2}$$

where we reserve the symbol Δ for differences in measurements between 77 and 300 K. The emf-free quantity $\Delta V(t)$ is independent of the placement of the voltage-tap leads (as long as the voltage-tap leads are mechanically fixed to prevent movement between the 77- and 300-K measurements). An example open-circuit waveform for one rotor cycle is shown in Fig. 2(b). An issue arises when one is seeking to measure $\Delta V(t)$ waveforms in the presence of a net transport current $|I_T| > 0$, as $V_{300\,\mathrm{K}}(t, I_T)$ is not available due to the inability to transport large currents through the stator in the normal-conducting state at 300 K. Hence, more generally, we define

$$\Delta V(I_T, t) = V_{77\,\mathrm{K}}(I_T, t) - V_{300\,\mathrm{K}}(0, t), \tag{3}$$

where $V_{300\,\mathrm{K}}(0, t)$ still captures the emf contribution assuming a static transport current.

While Eq. (2) allows us to examine the transient dynamics of the device during operation, the useful output of the device is its time-averaged dc voltage,

$$V_{\mathrm{dc}} = f \int_0^{1/f} V_{77\,\mathrm{K}}\, dt = f \int_0^{1/f} \Delta V\, dt, \tag{4}$$

where f is the frequency of rotation of the rotor. Note that at room temperature the integral of $V_{300\,\mathrm{K}}$ is zero as the device, when normal-conducting, is equivalent to a classical ac alternator with a linear resistivity.

Underneath the HTS stator tape, an array of seven Arepoc cryogenic Hall probes is mounted approximately 0.5 mm away from the tape surface, measuring the component of the magnetic field perpendicular to the tape, B_y.

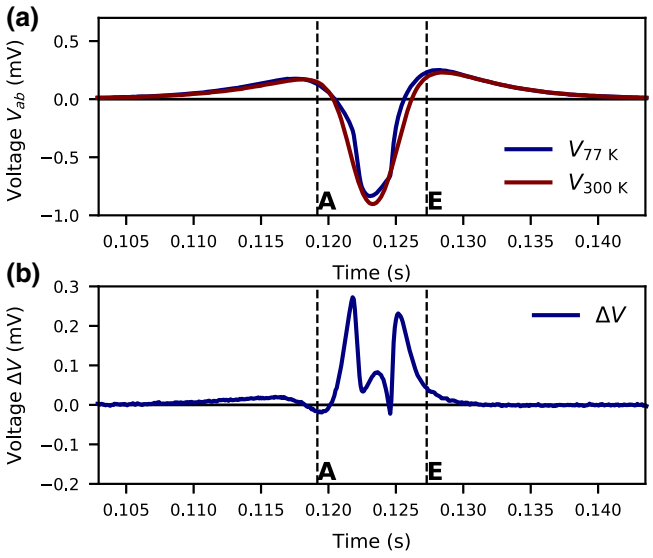

FIG. 2. (a) Comparison between 77- and 300-K voltage-pulse measurements with the dynamo operating at 12.33 Hz as the magnet transits the stator. (b) Voltage difference ΔV, as defined in Eq. (2), showing a clear dc bias in the 77-K waveform.

Again, we make measurements of the magnetic field at 77 K, $B_{77\,\mathrm{K}}$, and at 300 K, $B_{300\,\mathrm{K}}$. As the Nd-Fe-B magnet exhibits the same magnetization at these two temperatures, any difference between the measured magnetic fields must be caused by currents flowing in the HTS tape:

$$\Delta B(x, t) = B_{77\,\mathrm{K}}(x, t) - B_{300\,\mathrm{K}}(x, t) = \mu_0 H_y(x, t), \tag{5}$$

where H_y is the perpendicular auxiliary field due to the free currents in the conductor.

The rotor and stator assembly of the device is placed in a bath cryostat, with the 77-K measurements made following submersion in liquid nitrogen. Mechanical power to the rotor is provided through a G10 composite shaft connected to an external stepper motor at room temperature. The stepper motor gives a selection of rotational frequencies of 178, 255, 365, 520, 740, 1051, and 1490 rpm. Measurements are taken using a single magnet in the rotor assembly, such that there is a 1:1 relation between the motor speed and the frequency f of the applied magnetic field in the stator tape. At each rotor speed, the full I-V curve is examined by adjusting the net current flowing through the stator tape, using a 6680-A current supply (Agilent J04) to step the current in 2-A increments.

III. MODELING, MEASUREMENT, AND THEORY

To investigate the physics underlying the measured voltages and magnetic fields, it is necessary to build a model of the given system. First we must clearly establish the relationship between the measured values and the physical fields that underlie them. We start with the gauge-invariant

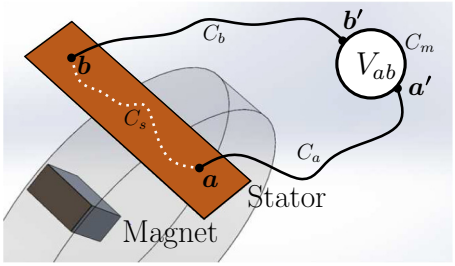

FIG. 3. HTS stator and attached voltage leads, forming the four sections of the Amperian loop C: through the sample, C_s; through the two leads, C_a and C_b; and through the meter, C_m.

form of the electric field,

$$\vec{E} = -\vec{\nabla}\psi - \partial_t \vec{A}, \tag{6}$$

where $\vec{\nabla}\psi$ is the gradient of the scalar potential, and $\vec{A}$ is the magnetic vector potential. As explained well by Clem [42], any measured voltage V_{ab}, such as $V_{300\,\mathrm{K}}$ or $V_{77\,\mathrm{K}}$, is given by the electric field in the meter itself. In the case of an ideal voltmeter, the active component is taken to be sufficiently small that $\partial_t \vec{A}$ is negligible, and the meter is affected only by the electrostatic potential $\vec{\nabla}\psi$ (see Fig. 3). Therefore the value of $\vec{E}$ in the meter can be solved for by solving for $\vec{\nabla}\psi$. As any integral of $\vec{\nabla}\psi$ between a' and b' is path-independent, it must be equivalent to the integral along the nearly closed loop made by the sample and the measurement leads between the same points a' and b'. Denoting the path through the leads as $C_l = C_a + C_b$ and the path through the sample as C_s, and assuming $\vec{E} = 0$ in the leads, we can define the measured voltage V_{ab} as

$$\begin{aligned} V_{ab} &= \int_{C_m} \vec{\nabla}\psi \cdot d\vec{l} = \int_{C_s} \vec{\nabla}\psi \cdot d\vec{l} + \int_{C_l} \vec{\nabla}\psi \cdot d\vec{l} \\ &= -\int_{C_s} \vec{E} \cdot d\vec{l} - \int_{C_l + C_s} \partial_t \vec{A} \cdot d\vec{l} \\ &= -\int_{C_s} \vec{E} \cdot d\vec{l} - d_t \iint_{S_s} \vec{B} \cdot d\vec{s}, \end{aligned} \tag{7}$$

where we note that while the integral through $C_l + C_s$ is not closed, since the contribution from C_m is missing, as the length of C_m tends to zero, this term captures the rate of change of the captured magnetic flux.

Re-examining the experimental logic behind Eq. (3), stating that $V_{300\,\mathrm{K}}$ is a measure of the emf, we can frame the approximation as a condition on the magnetic flux through the loop:

$$d_t \iint_{S_s} \vec{B}_{77\,\mathrm{K}} \cdot d\vec{a} = d_t \iint_{S_s} \vec{B}_{300\,\mathrm{K}} \cdot d\vec{a}. \tag{8}$$

We can not impose a more rigorous, local, or even weaker assumption on the fields at the different temperatures. Indeed, some local restrictions on B would invalidate Eq. (5).

With the approximation well defined, we may express ΔV using Eq. (7):

$$\Delta V = -\int_{C_s} \left(\vec{E}_{77\,\mathrm{K}} - \vec{E}_{300\,\mathrm{K}}\right) \cdot d\vec{l}. \tag{9}$$

Focusing our analysis on the symmetric plane bisecting the dynamo, we can capture the necessary physics without considering the nature of the integral paths. In the symmetric x, y plane, only currents into and out of the plane, J_z, need to be considered. This of course limits $\vec{E}$ to E_z as well. Furthermore, it can be shown that the assumption of reflection symmetry in the plane forces $\vec{\nabla}\psi$ to be constant over the plane, up to a choice of gauge. Therefore, the spatial variations in E_z can be attributed entirely to the changing vector potential $d_t A_z$. Hence, in the plane, $\vec{\nabla}\psi$ can be thought of as

$$\begin{aligned} \vec{\nabla}\psi(x,y,z,t)|_{z=0} &= \partial_z \psi(t) \\ &= -E_z(x,y,t) - d_t A_z(x,y,t), \end{aligned} \tag{10}$$

which leads to the fact that only the spatially averaged components of both E_z and $d_t A_z$ contribute to $\partial_z \psi$:

$$\begin{aligned} \partial_z \psi(t) &= \frac{1}{A} \int_\Omega \partial_z \psi(t)\, da \\ &= \frac{1}{A} \int_\Omega E_z(x,y,t) - d_t A_z(x,y,t)\, da \\ &= -E_{\mathrm{ave}} - d_t A_{\mathrm{ave}}. \end{aligned} \tag{11}$$

From Eq. (11), we can quickly examine Faraday's alternator, where, for a homogeneous normal conductor, $E = \rho J$ implies $E_{\mathrm{ave}} = \rho J_{\mathrm{ave}}$, i.e., Ohm's law. Then the ac alternator has a dc component proportional to the dc current flowing through the stator, and if that dc current is zero, then there is no dc output voltage. However, in the case of a superconductor, $E = \rho(J)J$ does not imply $E_{\mathrm{ave}} = \rho(J_{\mathrm{ave}})J_{\mathrm{ave}}$.

Looking back at Eqs. (2) and (9) and using the same assumptions, we can use Eq. (11) to define a similar comparison of states (superconducting versus normal) for $\partial_z \psi$:

$$\begin{aligned} \Delta\partial_z \psi(I_T,t) &= \partial_z \psi_{77\,\mathrm{K}}(I_T,t) - \partial_z \psi_{300\,\mathrm{K}}(0,t) \\ &= -E_{\mathrm{ave},\,77\,\mathrm{K}}(I_T,t), \end{aligned} \tag{12}$$

where, again, the spatially averaged electric field for zero net current at room temperature, $E_{\mathrm{ave},\,300\,\mathrm{K}}$, is equal to 0 V/m and the A-vector is the same at both room temperature and 77 K, i.e., $d_t A_{\mathrm{ave},\,77\,\mathrm{K}} = d_t A_{\mathrm{ave},\,300\,\mathrm{K}}$, which is true in the context of the full measurement loop, regardless of gauge as long as we assume Eq. (8).

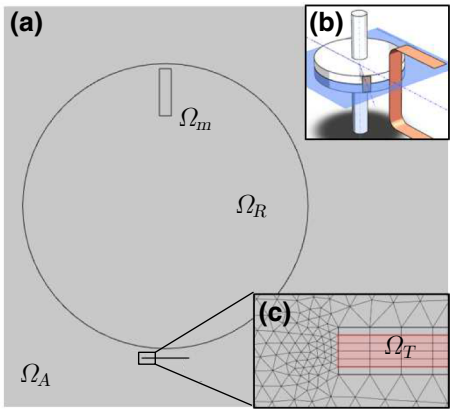

FIG. 4. (a) 2D model of the bisecting plane, with the air (Ω_A), rotor (Ω_R), tape (Ω_T), and magnet (Ω_m) domains. (b) Inset showing a 3D schematic illustration of the dynamo stator and rotor and the modeled bisecting plane. (c) Magnified view of the tape domain Ω_T and FE model mesh.

If we make the simple approximation that the three-dimensional (3D) system is translationally symmetric along the length of the magnet L, then the solution in the plane can be extrapolated and related to measurements:

$$\begin{aligned} \Delta V(I_T,t) &= \int_{-L/2}^{L/2} \Delta\partial_z \psi(I_T,t)\, dz, \\ \Delta V(I_T,t) &= -L \times E_{\text{ave, 77 K}}(I_T,t), \end{aligned} \tag{13}$$

where the lhs is measurable and the rhs can be calculated. For brevity, we refer to $E_{\text{ave, 77 K}}$ as simply E_{ave} from this point on.

IV. MODEL CONSTRUCTION

In order to calculate $E_{\text{ave}}(t)$, we must calculate the full solution for $E_z(x,y,t)$ in the modeled plane. To do this, we use the H-formulation form of the finite-element problem to solve Maxwell's equations. As argued, we take advantage of the device's reflection symmetry to reduce our problem to the 2D plane bisecting the stator and the rotor. In this arrangement, shown in Fig. 4(a), we define the x axis to be oriented along the width of the tape, the y axis to be oriented along its thickness, and the z axis to be out of the plane.

The 12-mm-wide superconducting layer is modeled as a 100-μm-thick domain, rather than using its real thickness of approximately 1 μm; this avoids the logarithmic singularity in the solutions for 2D conductors [43] and therefore improves convergence times [39,44]. The copper stabilizer of the tape is modeled as two 25-μm domains on the top and back surfaces of the superconducting domain. The resistivity of the copper is assumed to be that of electrical-grade material, $\rho_{\text{Cu}} = 0.19\ \mu\Omega\text{cm}$.

In the H-formulation, the problem of solving Ampère's and Faraday's laws is expressed in terms of the electric field $\vec{E}$, the free current density $\vec{J}$, and the auxiliary field $\vec{H}$. This gives Ampère's law,

$$\nabla \times \vec{H} = \vec{J}, \tag{14}$$

and Faraday's law,

$$\nabla \times \vec{E} = -d_t \vec{B}. \tag{15}$$

The finite-element model is then constructed using edge elements [37], which assign the degrees of freedom of the model to the tangential component of the auxiliary field $\vec{H}$. This satisfies a weak form of Stokes' theorem and defines J_z explicitly by the tangential components of $\vec{H}$. This explicitly satisfies Eq. (14) and also enforces current continuity.

Equations (14) and (15) are then linked by the appropriate choice of constitutive relations: firstly, the relation between the auxiliary field and the magnetic field,

$$\vec{B} = \mu_r \mu_0 \vec{H}, \tag{16}$$

where μ_r is the relative permeability, which is taken as 1, and secondly, the relationship between the current density and the electric field,

$$\vec{E} = \rho \vec{J}, \tag{17}$$

where ρ is the volumetric resistivity. To capture the behavior of the HTS material, we use the E-J power law [45,46],

$$\rho = \frac{E_0}{J_c(|\vec{B}|,\theta_B)} \left| \frac{\vec{J}}{J_c(|\vec{B}|,\theta_B)} \right|^{n-1}, \tag{18}$$

where E_0 is the characteristic electric field, typically chosen as 1 μV/cm, $J_c(|\vec{B}|,\theta_B)$ is the critical current density, θ_B is the angle of the magnetic field with respect to the normal to the tape, and n is the so called n-value which captures the steepness of the transition to the normal state and is taken to be 20. We take $J_c(|\vec{B}|,\theta_B)$ as the value measured experimentally in the SuperCurrent facility at Robinson Research Institute [47,48], which is shown in Fig. 5, and then normalize by the self-field critical current of the stator, $I_c = 293$ A.

To solve the problem of representing a moving magnet in the H-formulation formalism [49,50], we represent the field of the magnet as a sheet current J_m along the boundary $\partial\Omega_R$. To enforce this condition, we add a weak formulation condition to the finite-element problem,

$$\nabla \times \vec{H} = \vec{J}_m(\theta - \theta_R(t)) \text{ on } \partial\Omega_R, \tag{19}$$

where θ is the azimuthal angle, and J_m is rotated by θ_R to simulate the rotation of the magnet.

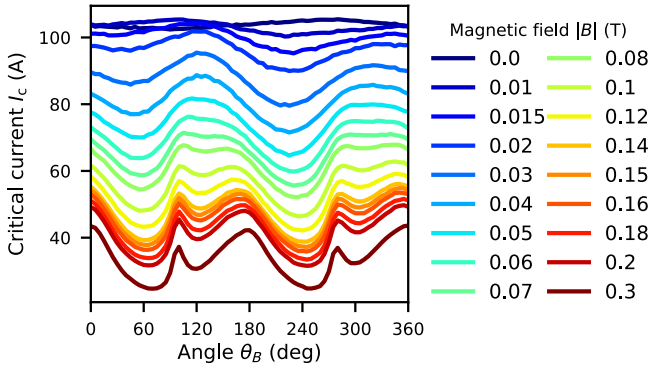

FIG. 5. Measured in-field $I_c(B,\theta)$ performance of 4-mm-wide SuperPower SCS4050 AP superconductor, which we scale to the 12 mm width used in our experiments.

To account for net transport currents I_T, we consider the external power supply to be an ideal current source. Therefore we restrict the currents in the tape to obey

$$I_T = \int_{\Omega_T} \vec{J} \cdot d\vec{a} = \oint_{\partial\Omega_T} \vec{H} \cdot d\vec{l}. \tag{20}$$

Finally, the whole model is bounded on $\partial\Omega_A$, taken to be 300 mm away from the center, where $\hat{n} \times \vec{B} = 0$.

Each model is run for a total of three cycles. During the first cycle, the transport current is arbitrarily distributed but is redistributed by the applied magnetic field, which has some effect on the output. However, on the second and third cycles the system is found to be periodic, and hence no further cycles are necessary. To capture the effect of frequency and transport current, we simply run the models with different rotational speeds of the shell current J_m and different values of I_T.

V. RESULTS

First we present measured dc values that highlight that the model agrees with experiment over a large range of parameters, but we do not test the local dynamics of the model directly. Next, transient electrical waveforms confirm that the model replicates the dynamics of the system. Finally, we present locally collected magnetic field data that confirm the dynamic spatial agreement between the model and experiment.

A. dc characterization

The HTS dynamo can be characterized as a simple voltage source, as shown in Fig. 1(b), with an open-circuit voltage V_{oc}, an internal resistance R_{int}, and a short-circuit current I_{sc}. Figure 6 presents dc (time-averaged) values from the electrical characterization of the experimental device and the FE model. I-V characteristics from the model [Fig. 6(a)] and from the experiment [Fig. 6(b)] are presented. From these I-V characteristics, the key idealized parameters V_{oc}, V_{oc}/f , I_{sc}, and R_{int} can be extracted, as shown in Figs. 6(c)–6(e), respectively.

Broadly speaking, the model reproduces the I-V behavior observed in the experiment. At every frequency, the slope of the curves in Figs. 6(a) and 6(b) is essentially linear, implying a constant internal resistance R_{int}, and the magnitudes of the values are clearly similar.

While the modeled V_{oc} includes a factor L from the extrapolation [see Eq. (13)], the short-circuit current I_{sc} should not. That is, as we extrapolate the model from the 2D plane, the amount of current is unaffected. Hence, Fig. 6(c) provides the most stringent test of the model's accuracy. From this we see that the model reproduces the behavior extraordinarily well, with only a 5% deviation from the experimental values for the five highest frequencies. To eliminate the factor L, which is the only geometric degree of freedom, we present a set of scaled values based on changing $L = 12.7$ mm in Eq. (13) to $L' = 10.2$ mm. This is done by fitting V_{oc} for the five matching frequencies from Fig. 6(c). Note that $L' < L$ is expected given the divergence of the field in three dimensions. Figures 6(d)–6(f) present both the results from the raw model and the scaled values.

One of the most widely accepted behaviors of HTS dynamos is a linear dependence of the output on frequency. This behavior is borne out in the models. Figure 6(d) compares the measured V_{oc} with values extrapolated from the model, showing that while the unscaled model overestimates the output, the linearity is indeed reproduced. To examine the behavior more closely, in Fig. 6(e) we normalize the output voltages by the rotational frequency, exaggerating the deviations from the linear behavior. We can see that the experimental data show a small scatter around what would be assumed to be a constant value, and hence an assumption of linearity is justified. This scatter is not present in the modeled data, however, showing a clear nonlinear component.

A central question about the device is the nature of the internal resistance, and whether it can be appropriately described in the context of the dynamic resistance effects reported elsewhere [51,52]. The scaled model and experimental data show tight agreement for the internal resistance of the device, including the downward trend in resistance per cycle for increasing frequency.

The interplay between V_{oc}, R_{int}, and I_{sc} highlights the fact that the dynamo does not have some simple explanation via flux transfer across the stator tape. For example, the simplest flux-transfer models would predict a constant flux per cycle. This is even more interesting when one considers that the internal resistance per cycle of the device not only drops but also drops faster than the flux transferred per cycle, as evidenced by the increasing I_{sc} with frequency.

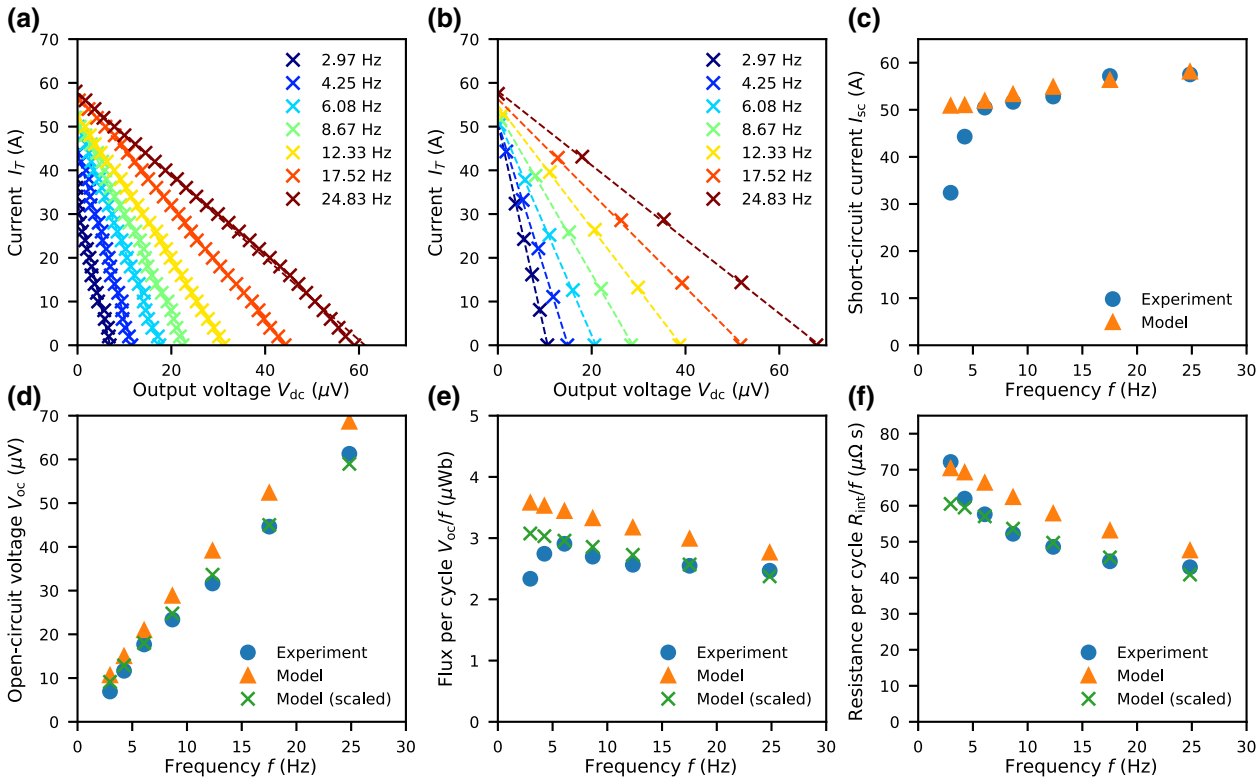

FIG. 6. Comparison of dc electrical characterization of the HTS dynamo for experimental and modeled values. (a) Modeled and (b) experimental I-V characteristics for various frequencies. (c) Modeled and measured short-circuit current I_{sc} versus frequency. (d) Comparison of measured, modeled, and scaled open-circuit voltages V_{oc} versus frequency f . (e) Frequency-normalized open-circuit voltage (flux per cycle) versus frequency. (f) Frequency-normalized internal resistance R_{int} versus frequency.

B. Transient characterization

The HTS dynamo is not a dc device, and transient behavior can be measured to test the model. Figure 7 shows several of the key ΔV waveforms obtained from the scaled models and experiment. All the qualitative features are replicated in the transient behavior of the models. Furthermore, quantitative agreement is again achieved using the scaled value for L', further indicating that no qualitatively important physical effects have been left out of the model.

Figures 7(a) and 7(b) show that, when normalized by frequency and plotted versus the rotor position θ_R, the open-circuit ΔV falls onto the same curve for all frequencies measured or modeled. The small deviations from linear scaling can be attributed to specific moments in the cycle. This indicates that while the frequency has an effect, as shown in Fig. 6, the effects are only small (but systematic) adjustments to a broadly similar behavior. Figures 7(a) and 7(b) show the key qualitative features of the rectification in the HTS dynamo, i.e., that it occurs primarily as the magnet enters **A** $\rightarrow$ **B** and when it exits **D** $\rightarrow$ **E**. This is seen in the two dominant peaks. Figures 7(a) and 7(b) also show some important qualitative differences: Fig. 7(a) shows a clear rise as the magnet approaches $\theta_R < 155^\circ$, but this rise and the subsequent dip are not present in the modeled values. This is the clearest example of how our approximation in Eq. (8) breaks down. However, the breakdown in the approximation does not obscure our ability to identify the dominant behaviors.

The appearance of the internal resistance can be seen in Figs. 8(c) and 8(d), which show how each ΔV waveform changes with increasing current through the stator. From these curves, we can see that the dynamic resistance appears as a reduction in the output voltage waveform. Not only is this reduction localized to the voltage-generating portion of the cycle, where the magnet is over the stator, but also the waveforms seem to peel away from each other at around point **B**. This peeling indicates that there is a portion of the cycle that does not experience the internal resistance, and that this portion reduces with increasing current. Furthermore, the changes in the middle of the waveforms between **B** and **D** clearly indicate that the initially (open-circuit) low output during these times is not due to a lack of dynamics, but rather is coincidental with the lack of a transport current.

A further question regarding the internal resistance is its apparently constant value for any given current and fixed frequency. This could simply be a coincidence, hidden by the dc time average used in Fig. 6. To avoid this,

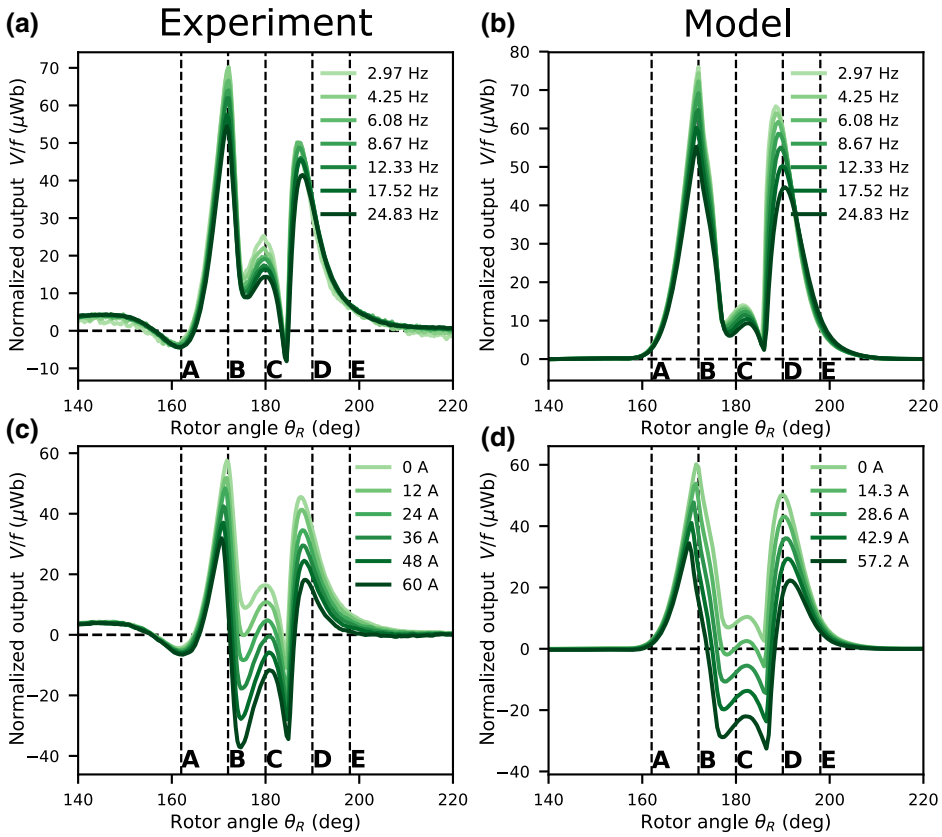

FIG. 7. Transient ΔV waveforms: measured, left column, and modeled (scaled), right column. The points marked **A**–**E** match those defined in Fig. 1(b). (a),(b) Open-circuit frequency-normalized ΔV versus rotor angle at several different frequencies. (c),(d) $\Delta V(I)$ waveforms for increasing transport current at 17.5 Hz.

we introduce the instantaneous resistance,

$$R_{\text{inst}} = \frac{V_{77\,\text{K}}(I,t) - V_{77\,\text{K}}(0,t)}{I} = L' \frac{E_{\text{ave}}(I,t) - E_{\text{ave}}(0,t)}{I}. \tag{21}$$

Figure 8 shows the (a) measured and (b) modeled values of R_{inst} versus the magnet position during each cycle. All curves follow the same nontrivial shape, just as the frequency-scaled open-circuit voltages in Fig. 7(a) collapse on each other. While we see some deviations between the model and the experiment, again we attribute this to a breakdown in our approximation in Eq. (8), and note that the amount of diamagnetically shielded flux must therefore be highly systematic.

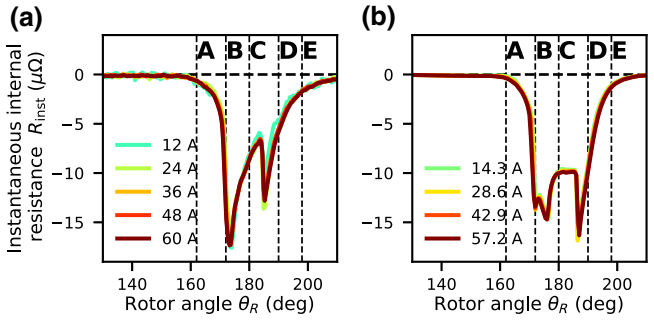

FIG. 8. Values of instantaneous resistance R_{inst} versus rotor angle θ_R for the transport currents reported in Fig. 7 for (a) measured data, and (b) scaled models.

C. Magnetic field

While dc values are critical for operational predictions, and transient behaviors allow us to confirm the behavior without taking the dc time average, all the results presented so far are obscured by the spatial averaging effect of comparing ΔV with E_{ave}; see Eq. (11). Ultimately, E_{ave} is the result of the spatial dynamics of the overcurrents inside the stator. Therefore, if claims are to be made as to the effects of the spatial distribution of these currents, then the model's spatial degrees of freedom need to be tested against experiment.

Figure 9 compares experimental and modeled values for the magnetic field difference ΔB, defined in Eq. (5), for $f = 17.52$ Hz (clockwise rotation). This is perpendicular to the stator's surface and taken along a line across the width of the stator and 0.5 mm behind it, as shown in Fig. 3. In the case of the experimental data, the contour plots linearly interpolate the values in between the seven sensors of the array. For the model itself, the data are taken along a line 0.5 mm from the back edge of the tape and are plotted as is. The x axis of the contours corresponds to the x position across the width of the tape, whereas the y axis is used to denote the angle of the rotor θ_R. Figure 9

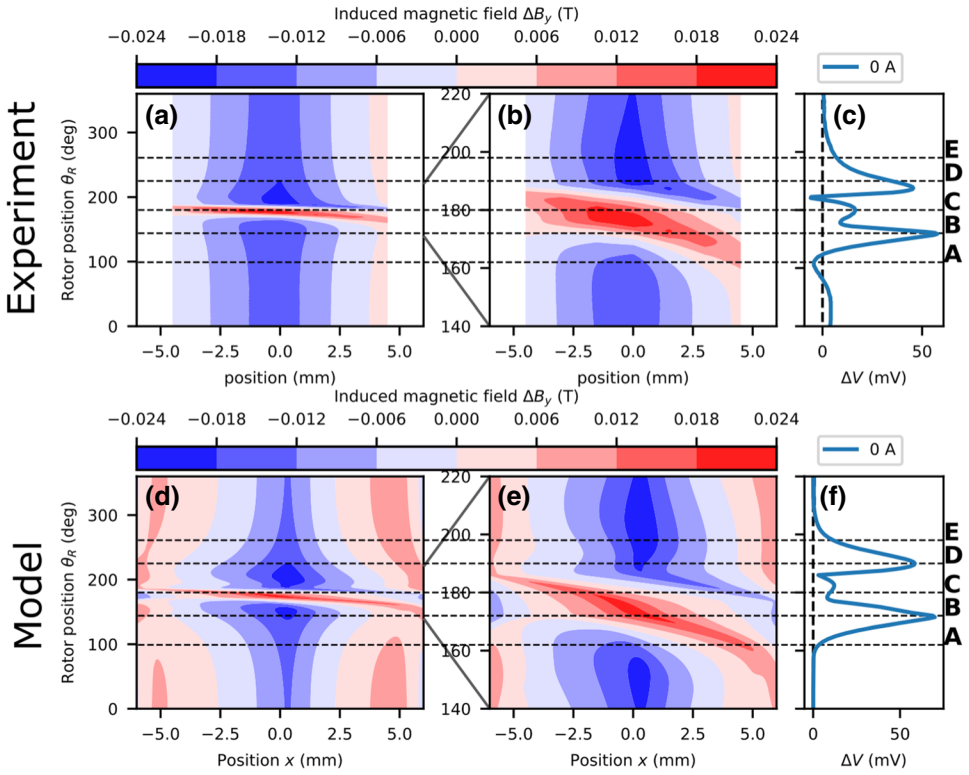

FIG. 9. Induced magnetic field ΔB across the width of the tape (x axis) versus rotor angle θ_R (y axis) for 17.52-Hz clockwise rotation (right to left). (a) Measured values from seven Hall probes at 0.5 mm from the stator. (b) Enlarged view of (a). (c) Measured ΔV for (b). (d) Modeled data for the full width of the tape, at the same distance from the tape. (e) Enlarged view of (d). (f) Scaled ΔV for (e).

shows the full cycle of the dynamo, which is dominated by the remnant magnetization as the overcurrents relax under flux creep. Here we see the largest disagreement between the model and experiment, with the remnant-magnetization profiles being strikingly different. However, the aim of the model is not to reproduce the flux-creep effects in these devices, and the index n is set to 20 as the model appears insensitive to its value.

Figure 10 presents ΔB for the 17.52-Hz data, enlarged to focus on the induced magnetic field during the magnet's transit, for several different values of the net transport current I_T. We see excellent agreement between the model and the experiment during the dynamics of the magnet's transit over the tape. Inspecting Fig. 10 further, we can identify several features during the transit. We can see the magnet enter from the right-hand side of the plot, as the induced current precedes the applied magnetic field. As the magnet travels across the conductor, these shielding currents erase the remnant magnetization in the conductor. As the magnet leaves, this remnant magnetization reasserts itself, with a characteristic jump in intensity between **D** and **E**, as the magnetic field suppression of $J_c(|\vec{B}|, \theta_B)$ subsides. Finally, with the magnet clear of the conductor, we see a slow decay of these currents into the final remnant magnetization.

Looking at Fig. 10, we notice that the response is almost unchanged with the addition of the transport current. The easiest way to identify that there is a change at all is to focus on the center of the remnant magnetization as it shifts to the left. Over the I-V characteristic of the device, from $I_T = 0$ to $I_T = I_{sc}$, we see essentially no change in the shielding behavior of the device. And yet, the ΔV waveforms in Figs. 10(c) and 10(f) clearly capture the reduction in output voltage.

Ultimately it is our goal to reconstruct the dynamics of the device, which is determined by the dynamics of the underlying current flows $\vec{J}$. As ΔB is the magnetic field induced by those currents, we can draw the desired conclusions from the calculated current density $\vec{J}$ with some certainty, given the correspondence between the measured and modeled values of ΔB.

D. Current maps

Figure 11 shows several contour plots, constructed similarly to Fig. 9, of the current density flowing through the tape in each part of the cycle for both HTS and copper stators. Note that the current density here is the sheet current density defined by

$$K_z = \int_h J_z \, dy, \tag{22}$$

where h is the thickness of the tape. During the transit of the magnet, the current density in the high-temperature superconductor is significantly higher than the critical current of the tape, i.e., $J_z > 1.5 J_c$. This correlates with the fact that the measured voltages imply that the stator has been driven a considerable distance into the flux-flow regime. It also implies that the real device has a current distribution significantly different from any prediction using

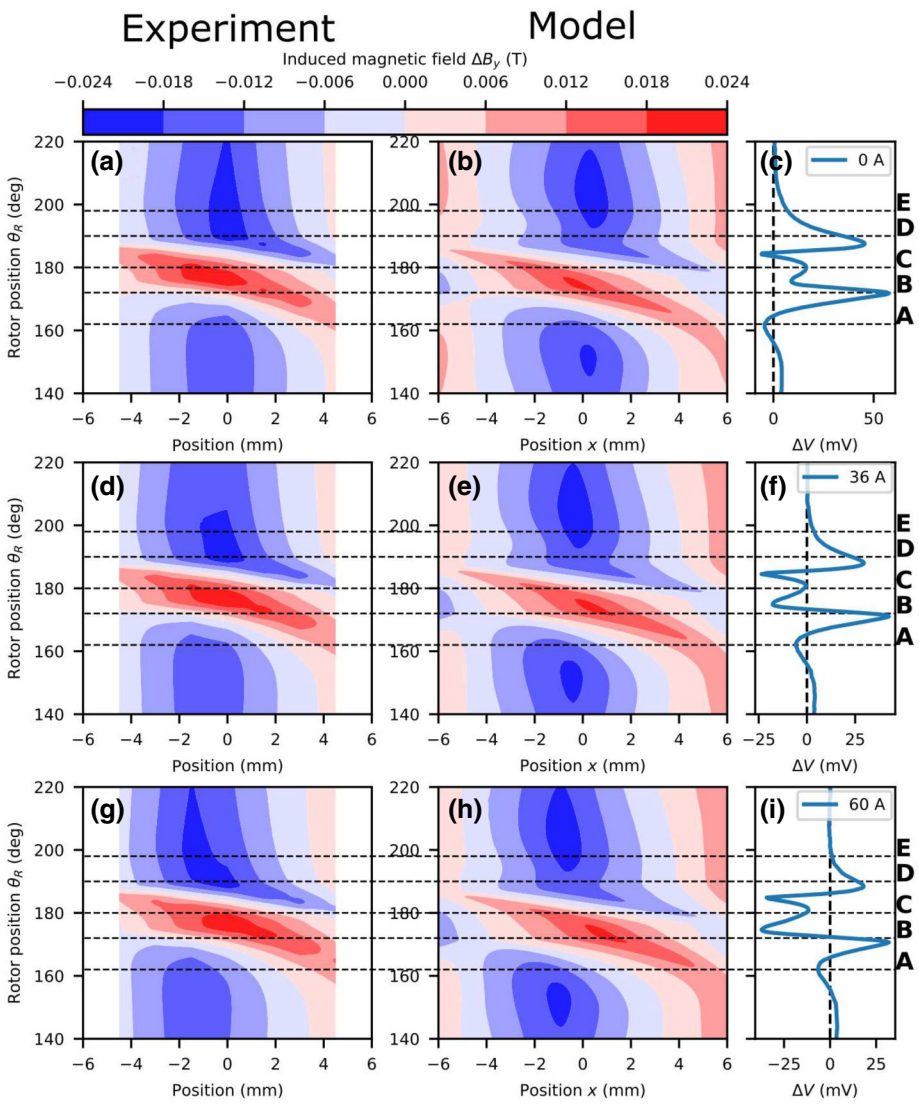

FIG. 10. Contour plots of induced magnetic field ΔB versus position across the tape width (x) and the rotor angle θ_R for measured and modeled values, with several net transport currents and 17.52-Hz clockwise rotation (right to left). (a),(b) Measured and modeled ΔB, respectively, for $I_T = 0$. (c) Measured ΔV for $I_T = 0$. (d),(e) Measured and modeled ΔB, respectively, for $I_T \approx 0.5 I_{sc}$. (f) Measured ΔV for $I_T \approx 0.5 I_{sc}$. (g),(h) Measured and modeled ΔB, respectively, for $I_T \approx I_{sc}$. (i) Measured ΔV for $I_T \approx I_{sc}$.

Bean's critical-state model, which would impose the limit $J_z \leq J_c$. In contrast, the current distribution in the copper stator [Figs. 11(e) and 11(f)] is simply a scaled multiple of the local emf in Fig. 11(g). Given the similarity between the emf in the high-temperature superconductor [Fig. 11(c)] and in the copper [Fig. 11(g)], we can also conclude that the stator dynamics is dominated by the applied magnetic field for the majority of the magnet's transit. As the conductor is primarily in the flux-flow regime, the shape of the electric field is essentially set by the rate of change of the applied magnetic field, via Faraday's law.

The source of the small difference between the emfs in the copper and in the high-temperature superconductor [Figs. 11(c) and 11(g), respectively] can be seen by examining the current densities [Figs. 11(b) and 11(f)]. From this, we see why it is that the HTS dynamo is capable of generating a nontrivial E_{ave}. That is, at every moment of the cycle, the current densities must sum to the total transport current; in this case, $I_T = 0$. However, even though the HTS is driven by the same applied emf, E_{ave} is not constrained to equal zero, as in the normal conductor, [Figs. 11(e) and 11(f)].

Locally speaking, the output emf of the dynamo, as a source of electrical energy for a connected load, must be associated with the eddy current underneath the magnet (the red forward current that transitions from right to left), as it has the correct polarity. We can also note that the device is also fundamentally dissipative: no currents ever experience a negative power, i.e., $EJ \not< 0$. Note that the output of the device naturally drives current in the backward direction.

Further inspection of Fig. 11(c) shows that the magnet continues to provide the desired emf for the entire transit, as one would have predicted from a normal spot or flux-transfer model in the low-T_c superconducting (LTS) case. However, unlike the case for a LTS dynamo, the current under the magnet as it transits is considerably larger, and must return in order to maintain the current constraint. It is

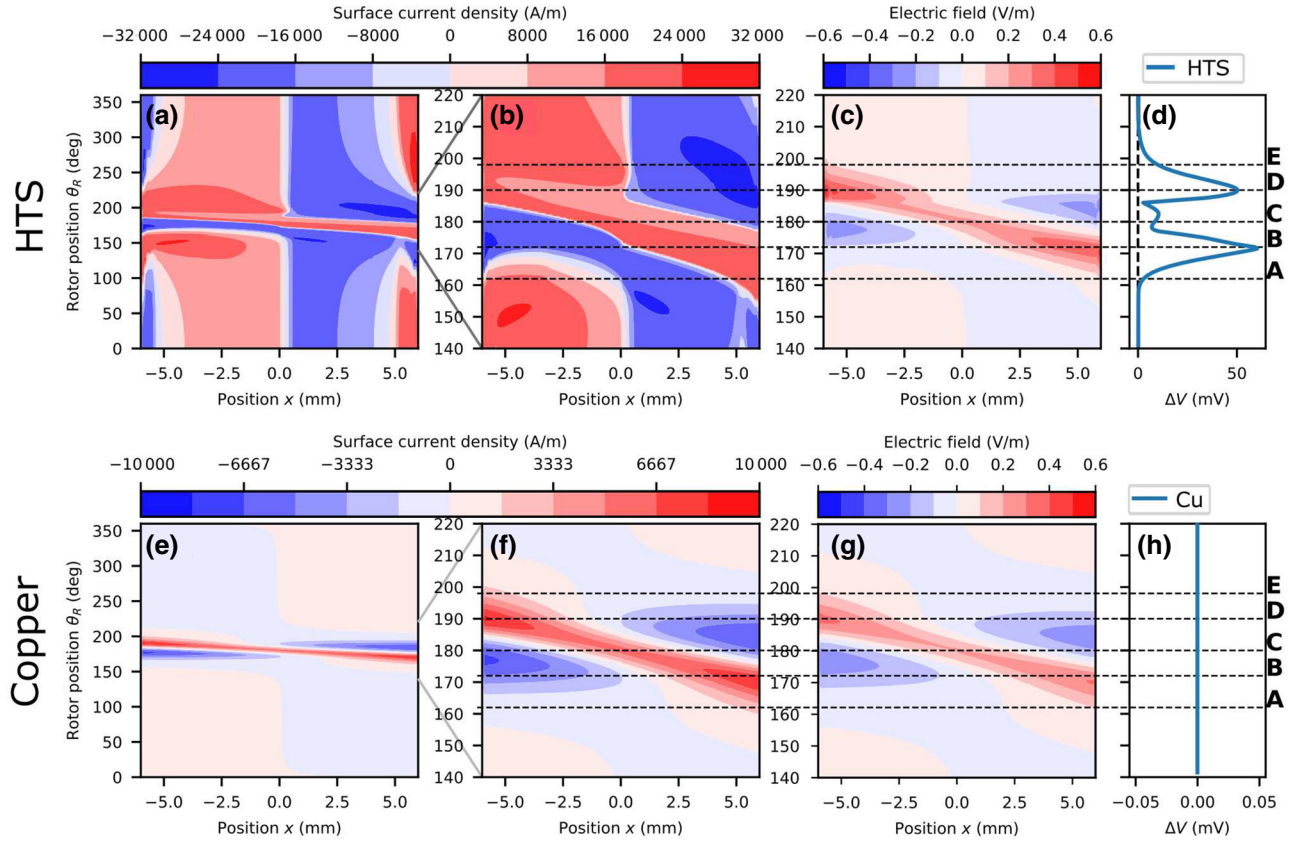

FIG. 11. Modeled sheet current density and electric field in superconducting (a)–(d) and normal (e)–(h) stators versus position x across the width of the tape and rotor angle θ_R for 17.52-Hz clockwise rotation (right to left) in open-circuit condition. (a),(e) Sheet current density for full cycle. (b),(f) Enlarged views of the sheet current density during the magnet's transit. (c),(g) Enlarged views of the local electric field E_z in the sheet. (d),(h) Corresponding plots of the modeled ΔV, which is equal to zero for copper. The dashed lines highlight key magnet positions.

this return current that both reduces the output between **B** and **D** and also becomes the driven current I_T.

Figure 12 shows a snapshot of the current and electric field distributions across the width of the tape, for copper and the high-temperature superconductor, at position **C** in the cycle for varying net transport currents. For copper, Fig. 12(a), we see the expected curves, where the positive peak electric field is under the magnet, and the current densities are simply scaled versions of the electric field profile. For increasing current, the current distributions in copper shift uniformly downward, resulting in the expected resistive E_{ave}. For the high-temperature superconductor, we observe that the shape of E_z is broadly similar for each current (as well as to that for copper), again reinforcing the observation that the shape of the electric field is predominantly determined by the applied magnetic field via Faraday's law. Unlike the case for copper, increasing net currents I_T are achieved by shifting the turning points of the current distribution J_z inward. However, the effect of changing the position of the turning points of the current, combined with the observation that the shape of E_z is broadly similar each time, leads to the simple conclusion that the average electric field is whatever it needs to be in order to satisfy the current constraint on the system. Therefore the internal resistance of the HTS dynamo corresponds to a reallocation of the applied local emf from the driving direction (a forward eddy current under the magnet) to the output direction (a return eddy current around the magnet).

Figures 13(a)–13(c) show how the eddy currents redistribute in order to accommodate the transport current I_T at three different positions along the I-V characteristic, matching the ΔB plots presented in Fig. 10. Here it is useful to distinguish between eddy currents driven by the magnet and the remnant magnetization currents that these eddy currents relax into after position **E**. If we focus on rotor positions before the magnet's transit, the transport current is asymmetric with respect to the forward and backward remnant currents, which is similar to the case of a dynamic resistance. As the magnet enters at **A**, the remnant current, including the transport current, is pushed to the right of the conductor, and we see that the forward eddy current under the conductor makes its way across the width. The fact that there is no location in the conductor where the current does not at some point flow in the

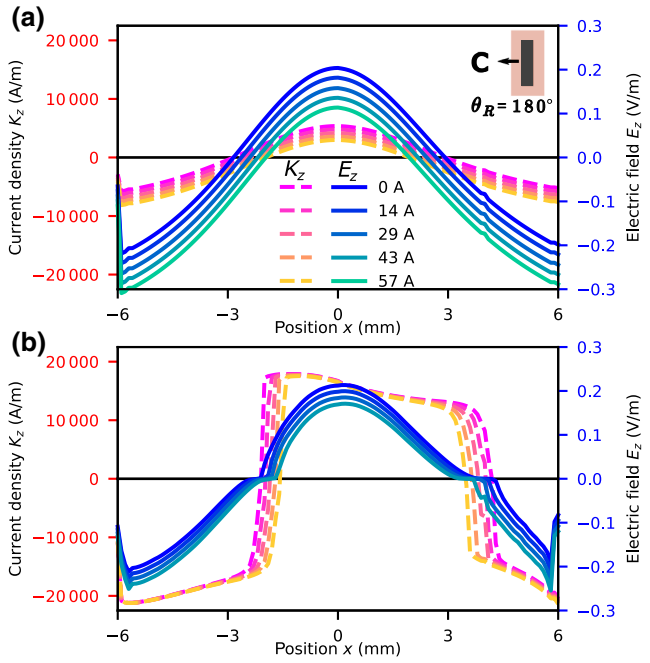

FIG. 12. Current (dashed lines) and local electric field (solid lines) from $I_T = 0$ (dark shades) to $I_T = I_{sc}$ (light shades) versus position x across the width of the tape, for copper (a) and high-temperature superconductor (b) at rotor position **C**. Data are presented for 17.52 Hz. The magnet position is illustrated as viewed from the Hall array.

backward direction distinguishes this situation from simple dynamic resistance.

An increased transport current displaces the forward remnant current shown in red. Because this system is cyclical, and the current is kept constant, the competition (loss) between the transport current and remnant current is not apparent at the start of the cycle. Also, we see that the backward eddy current underneath the magnet decreases in size (as a fraction of the conductor width) as the transport current is increased, which can also be seen in Fig. 12. This decrease in size reduces the amount of the applied emf that is captured in the driving direction, and instead we see it picked up in the backward direction as transport dissipation, or $R_{\rm int} \times I_T$.

As we have previously noted from Fig. 7, the internal resistance does not appear uniformly across the cycle. Instead, we can see parts of the cycle that experience very little dynamic resistance. This can be inspected by following the dashed line for **B** through all the plots in Fig. 13, where we see that the sharp increase in the dynamic resistance corresponds to the elimination of subcritical currents in the stator. Once the stator is full of overcritical current, the competitive effect between the forward and backward eddy currents leads to the internal resistance. This leads to the conclusion that there is some other smaller mechanism for the internal resistance that is in play before **B**.

To examine this, we show in Fig. 14 the sheet current and electric field for both copper and the high-temperature superconductor when the rotor is halfway between positions **A** and **B**, denoted by $\mathbf{A}^+$, across the whole I-V curve. For copper, Fig. 14(a), we see the effect of the magnet entering from the right and currents returning on the left, with a uniform shift up the y axis for increasing I_T. In complete contrast, Fig. 14(b) shows that the current distribution in the high-temperature superconductor accommodates the additional I_T by broadening in the x-axis direction, thus "filling in" the subcritical region on the left-hand side of the stator. This leaves the local emf from the applied magnetic field unchanged with current. It is clear from Fig. 13(d) that there should be some small internal resistance at this position, which can be identified with the smaller electric field lobe [identified by the blue arrow in Fig. 14(b)] in the center of the tape. This smaller lobe of the electric field corresponds to the remnant magnetization being forced out of the tape, and constitutes a completely different resistive mechanism from the one seen between positions **B** and **D**.

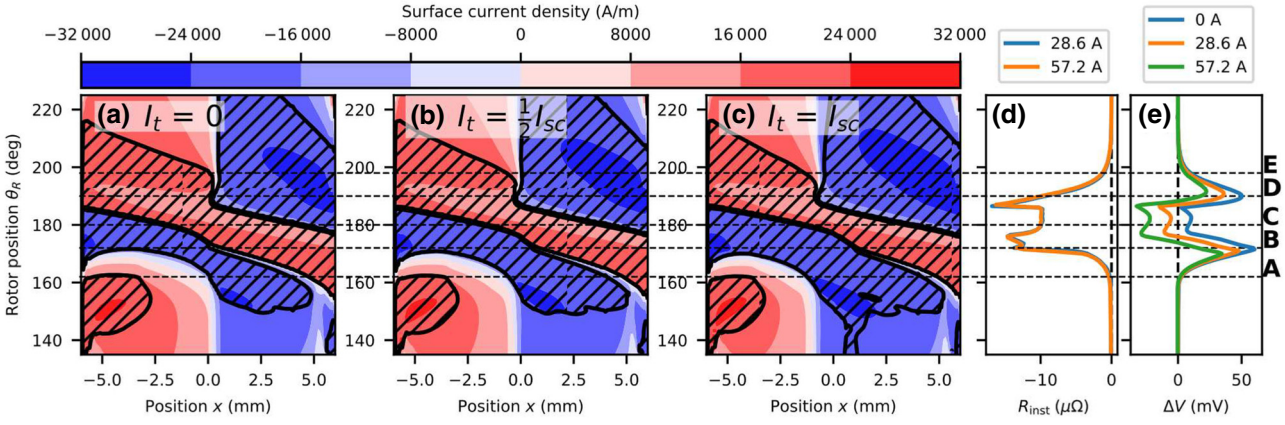

FIG. 13. Modeled current contours, $R_{\rm inst}$, and ΔV for several currents at 17.52 Hz; the cross-hatched regions identify $J > J_c$. (a) $I_T = 0$. (b) $I_T = (1/2)I_{sc}$. (c) $I_T = I_{sc}$. (d) $R_{\rm inst}$. (e) ΔV.

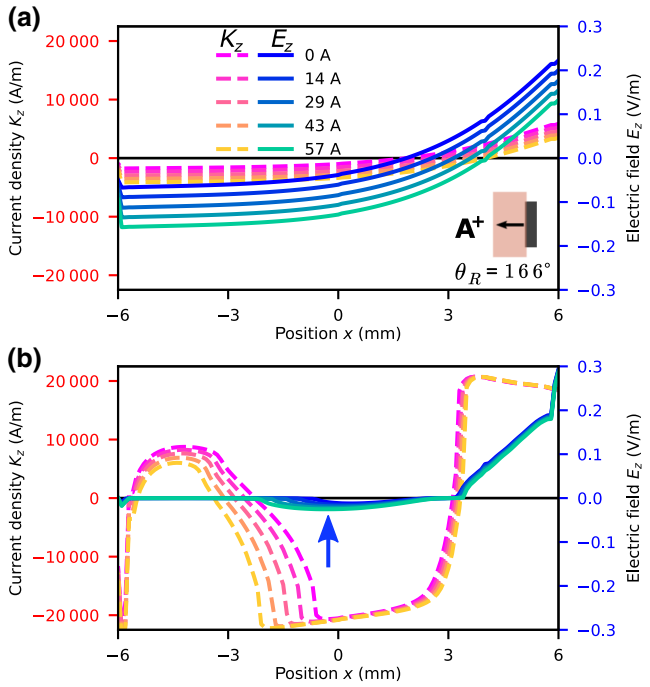

FIG. 14. Sheet current density K_z (dashed lines) and local electric field E_z (solid lines) along the 17.5-Hz I-V curve from $I_T = 0$ (dark shades) to $I_T = I_{sc}$ (light shades) versus position x across the width of the tape, taken for the rotor position $\mathbf{A}^+$, halfway between positions **A** and **B**, at $\theta_R = 166°$. Data are presented for 17.52 Hz. The magnet position is illustrated as viewed from the Hall array.

VI. DISCUSSION

A. Origin of the dc voltage V_{oc}

The arguments presented here revolve around three equations, Eqs. (15), (18), and (20), and how they interact to give E_{ave}. While it is absolutely true that the A-vector must be cyclical in these conditions, the currents that flow in response to the local electric field can give rise to nontrivial solutions for $\vec{\nabla}\psi$. By examining Fig. 12, we can see that the shape of the electric field is essentially the same regardless of the transport current, only shifting up and down to match the current constraint. This phenomenon is fundamentally different from that in the equivalent conventional dynamo, where the current constraint also maintains zero voltage. However, this story does not hold when there are still subcritical regions of the tape. When there is still room for the transport current to displace subcritical currents, the penetrated magnetic field contributes only to the driving direction (forward current under the magnet). This situation is likely to be much more similar to the normal spot operation seen in LTS dynamos [53], where the penetrated flux can migrate in penetrated normal zones.

The mechanism here should have some bearing on the mechanism of other flux pumps. For HTS rectifier-type flux pumps, Geng and Coombs [19] give an explanation in terms of flux linkage and the movement of the electric central line. As the HTS rectifier is based on a dynamic resistance switch that rectifies an applied ac emf, the movement of the central line of the electric field is very much akin to the movement of the electric field distributions in Fig. 12. The situation in the dynamo is of course complicated by the fact that the applied emf and the rectifying emf are one and the same. What does not have an analogue in the model of Geng and Coombs is the secondary resistive or generative mechanism highlighted in Fig. 14. In the rectifier, the only way to link the applied flux into the load is to create the kind of current competition that we see between positions **B** and **D**.

We find no evidence that the results presented here require any exotic physics, such as magnetic flux coupling (Wang and Coombs [34]). Two major points support this: (i) the work of Wang and Coombs refers to a rotationally symmetric system where an azimuthal voltage cannot be defined, let alone adapted to results for the dynamo; and (ii) the results presented by Wang and Coombs do not use a $J_c(|\vec{B}|, \theta_B)$ function, and so the equations solved cannot be affected by the dc offset of the magnetic field as claimed by those authors. Even if this is disputed, our results in Ref. [12] clearly show that a dc voltage can be achieved by a system with zero dc magnetic field sensitivity.

B. Output voltage versus current, R_{int} vs V_{oc}

The internal resistance of the HTS dynamo can be conceptualized as a dc dynamic resistance[3], akin to what is seen with dc transport currents in purely oscillatory magnetic fields [51]. To explain the rest of the I-V curves, given the gradient of the curve $R_{int} = R_{dyn}$, we have two options for the additional physics: to fix I_{sc} as some fundamental property of the system, or to relate V_{oc} to R_{int} via some underlying mechanism.

As argued in Sec. D, we see that the internal resistance is generated by competition between the transport current and the driven eddy current. Figure 12 shows that the shape of the electric field is largely unchanged by I_T. Rather, we argue that $\partial_z\psi$ is determined at any given time so that it is the shift of E_z that solves Eq. (20). Therefore, we must conclude that the correct interpretation is that V_{oc} and R_{int} must be understood with respect to the same underlying mechanism that generates E_{ave} in general, although this is not true before position **B**, as seen in Fig. 14, where the resistive mechanism is related to the movement of remnant magnetization rather than to a reallocation of the applied emf. This secondary smaller mechanism is again similar to that described by Mawardi [54] for LTS dynamos.

C. Short-circuit current I_{sc}

Given the relationship between R_{int} and V_{oc}, we see that I_{sc} is not a fundamental parameter of the system. In fact, this behavior makes sense with respect to the definition

of I_{sc} used here, where it is a dc property of an otherwise dynamic device. Nothing particularly special happens at any given moment of the cycle when I_{sc} is flowing through the tape. Rather, I_{sc} simply happens to be the current where the time average of the output happens to be zero. If one considers a dynamic definition of I_{sc}, using voltage rather than current control, one then naturally asks what the relationship between this dynamic definition and the dc short-circuit current would be.

While we leave this point for future work, it does highlight that we would expect the load reactance to play some role in the rectification effect. This also explains the experimental results presented here in Fig. 6 for the two lowest frequencies, 2.97 and 4.25 Hz, where the electronic load has insufficient inductance to oppose the small changes in the net current driven by the magnet as it passes the stator at a relatively slow speed. We also take the view that in Fig. 6(c) the trend must approach zero at zero frequency, as the plot will invert to the opposite polarity if the rotational direction is inverted, a behavior that the experimental data here seem to bear out. This provides some motivation for a model with an inductive boundary condition, rather than the infinite reactance used here. Ultimately, most practical magnets will have an inductance sufficiently high to appear essentially infinite to the dynamo.

D. Resistivity versus current

One of the primary observations about the reported HTS dynamos is their linear I-V characteristic. In complex systems, something can be linear for two reasons: (i) the underlying mechanism is linear, and superposition maintains the linearity in the emergent behavior, or (ii) the effect in question is interrogated over only a small part where it appears linear. In the case of the HTS dynamo, it is safe to say the underlying behavior is not linear, and therefore case (i) can be rejected.

We must conclude that the dynamos built so far explore only a small portion of some underlying behavior. We show here, for example, that the internal resistance is constant not only in the dc values, but also when expressed instantaneously at every moment of the cycle. However, the difference in the behavior of the device between open-circuit and closed-circuit conditions is very small. In fact, the qualitative behavior of the device is the same for all currents. If we focus on Fig. 12, we can see that shape of the electric field across the width of the conductor is unaffected by the introduction of a transport current. Consider how this curve moves, upward or downward, which corresponds to a change in the output voltage $\partial_z \psi(t)$. We can see that it is the gradient of the applied magnetic field, at the turning points of the current, that determine the change in voltage for a given change in current.

Figure 13 shows that the turning points of the sheet current K_z do not change very drastically over the I-V curve of the device. That is to say, the dynamo explores only a small section of the applied local emf when deciding its turning points. Hence, while the overall output of the device is a function of the total applied local emf, the behavior when the current is changed samples only the applied emf at the locations of the turning points. Therefore, when the current is changed, only a small section of the local emf is explored, over which it must appear linear.

To test this further, we propose experiments using far wider stators than those explored so far, or using parallel stators to create multiple return paths. Wider stators can carry more current overall, broadening the space within which the turning points of the current can be pushed. For sufficiently large or sufficiently high-current stators, we would expect a nonlinear I-V characteristic, as the local emf is probed at different locations [55].

E. Partial magnetic field penetration

The second behavior that prompts us to suggest wider stators is the observation that for some part of the cycle, the internal resistance is an order of magnitude lower even while rectified output is being generated. This can be seen in Fig. 7 and by inspecting the instantaneous resistance in Fig. 8 between **A** and **B**. First, we observe the fact that the applied magnetic field fully penetrates the whole tape for most of the magnet's transit. However, this is a geometric effect; a sufficiently wide stator would always have some region that was in the shielded regime, or parallel stators could act as return paths while not under a magnet. We see that the internal-resistance effect when remnant magnetization is being displaced is quite different from that when the transport current is competing with the driven eddy currents. While the output E_{ave} at the start of the transit is unaffected by an increasing transport current, the loss associated with the competition between the magnetization currents and the transport current is likely to be seen in the tail of the internal resistance past **E**; see Fig. 8. That is, as the driven eddy currents relax into the remnant magnetization, the presence of a transport current reduces the output. If this mechanism results in a significantly lower drop in ΔV, then large stators should have significantly improved short-circuit currents for a given magnet geometry.

VII. CONCLUSION

A predictive and powerful model of the HTS dynamo is presented, validated against experiments, and interrogated. The agreement between the model and the experimental data clearly indicates that inclusion of the nonlinear E-J characteristics of the HTS film has a profound effect. This nonlinearity gives rise to the dc voltage, as it breaks the oft-overlooked symmetry in eddy-current effects that is given by Ohm's law. The effects of this are seen at several levels of the analysis: dc quantities, transient voltage waveforms, and locally measured induced magnetic field distributions.

The model's dynamics can be interrogated for insights into its driving principles. Here, we outline how the local applied magnetic field across the HTS stator is rectified by the nonlinear E-J characteristics of the HTS material in the flux-flow regime. Furthermore, we show that the link between this rectified output and the transport current through the stator is predominantly caused by the competition between the transport current and the driven eddy current caused by the magnet's transit.

Finally, we identify a partially critical regime where the stator is only partially penetrated by the applied magnetic field. While we attribute a small resistance to the competition between the transport current and the magnetization currents in this regime, this resistive mechanism is much smaller than when the stator is fully penetrated by the applied magnetic field. Logically, we conclude that much lower internal resistances can be achieved by increasing the stator width sufficiently that the stator is never fully penetrated during the cycle of the device.

All data are provided in full in the results section of this paper.

ACKNOWLEDGMENTS

The authors would like to thank Dr. Stuart Wimbush for providing J_c data for the SuperPower tape. Financial support for this work was provided by the New Zealand Ministry of Business, Innovation and Employment (MBIE) via Grant No. RTVU1707, and the NZ Royal Society via Grant No. MFP-VUW1806. M.A. acknowledges financial support from the EPSRC via Grant No. EP/P020313/1.

[1] C. Hoffmann, D. Pooke, and A. D. Caplin, Flux pump for HTS magnets, IEEE Trans. Appl. Supercond. **21**, 1628 (2011).

[2] T. A. Coombs, J. F. Fagnard, and K. Matsuda, Magnetization of 2-G coils and artificial bulks, IEEE Trans. Appl. Supercond. **24**, 8201005 (2014).

[3] Z. Jiang, K. Hamilton, N. Amemiya, R. A. Badcock, and C. W. Bumby, Dynamic resistance of a high-T_c superconducting flux pump, Appl. Phys. Lett. **105**, 112601 (2014).

[4] J. Geng and T. A. Coombs, Mechanism of a high-T_c superconducting flux pump: Using alternating magnetic field to trigger flux flow, Appl. Phys. Lett. **107**, 142601 (2015).

[5] J. Geng, B. Shen, C. Li, H. Zhang, K. Matsuda, J. Li, X. Zhang, and T. A. Coombs, Voltage-ampere characteristics of YBCO coated conductor under inhomogeneous oscillating magnetic field, Appl. Phys. Lett. **108**, 262601 (2016).

[6] J. Geng, K. Matsuda, L. Fu, J.-F. Fagnard, H. Zhang, X. Zhang, B. Shen, Q. Dong, M. Baghdadi, and T. A. Coombs, Origin of DC voltage in type II superconducting flux pumps: Field, field rate of change, and current density dependence of resistivity, J. Phys. D **49**, 11LT01 (2016).

[7] C. W. Bumby, Z. Jiang, J. G. Storey, A. E. Pantoja, and R. A. Badcock, Anomalous open-circuit voltage from a high-T_c superconducting dynamo, Appl. Phys. Lett. **108**, 122601 (2016).

[8] C. W. Bumby, R. A. Badcock, H.-J. Sung, K.-M. Kim, Z. Jiang, A. E. Pantoja, P. Bernardo, M. Park, and R. G. Buckley, Development of a brushless HTS exciter for a 10 kW HTS synchronous generator, Supercond. Sci. Technol. **29**, 024008 (2016).

[9] S. Lee, W. Kim, Y. Kim, J. Lee, S. Park, J. Lee, G. Hong, S. Kim, J. Han, Y. J. Hwang, and K. Choi, Persistent current mode operation of a 2G HTS coil with a flux pump, IEEE Trans. Appl. Supercond. **26**, 0606104 (2016).

[10] A. M. Campbell, A finite element calculation of flux pumping, Supercond. Sci. Technol. **30**, 125015 (2017).

[11] K. Hamilton, A. E. Pantoja, J. G. Storey, Z. Jiang, R. A. Badcock, and C. W. Bumby, Design and performance of a "squirrel-cage" dynamo-type HTS flux pump, IEEE Trans. Appl. Supercond. **28**, 5205705 (2018).

[12] R. C. Mataira, M. D. Ainslie, R. A. Badcock, and C. W. Bumby, Origin of the DC output voltage from a high-T_c superconducting dynamo, Appl. Phys. Lett. **114**, 162601 (2019).

[13] A. Ghabeli and E. Pardo, Modeling of airgap influence on DC voltage generation in a dynamo-type flux pump, Supercond. Sci. Technol. **33**, 035008 (2020).

[14] C.-S. Lee, B. Jankó, I. Derényi, and A.-L. Barabási, Reducing vortex density in superconductors using the 'ratchet effect', Nature **400**, 337 (1999).

[15] M. P. Oomen, M. Leghissa, G. Ries, N. Proelss H. Neumueller F. Steinmeyer, M. Vester, and F. Davies, HTS flux pump for cryogen-free HTS magnets, IEEE Trans. Appl. Supercond. **15**, 1465 (2005).

[16] T. Nakamura, M. Sugano, T. Doi, and N. Amemiya, Flux pumping effect of HTS films in a traveling magnetic field, IEEE Trans. Appl. Supercond. **20**, 1033 (2010).

[17] Z. Bai, C. Chen, Y. Wu, and Z. Zhen, Effect of various pulse wave forms for pulse-type magnetic flux pump, Cryogenics **51**, 530 (2011).

[18] W. Wang, F. Spaven, M. Zhang, M. Baghdadi, and T. Coombs, Direct measurement of the vortex migration caused by traveling magnetic wave, Appl. Phys. Lett. **104**, 032602 (2014).

[19] J. Geng and T. A. Coombs, Modeling methodology for a HTS flux pump using a 2D H-formulation, Supercond. Sci. Technol. **31**, 125015 (2018).

[20] J. D. D. Gawith, J. Ma, B. Shen, C. Li, J. Yang, Y. Öztürk, and T. A. Coombs, An HTS power switch using YBCO thin film controlled by AC magnetic field, Supercond. Sci. Technol. **32**, 095007 (2019).

[21] A. He, C. Xue, and Y.-H. Zhou, Switchable reversal of vortex ratchet with dynamic pinning landscape, Appl. Phys. Lett. **115**, 032602 (2019).

[22] J. Geng, C. W. Bumby, and R. A. Badcock, Maximising the current output from a self-switching kA-class rectifier flux pump, Supercond. Sci. Technol. **33**, 045005 (2020).

[23] K. S. Haran, S. Kalsi, T. Arndt, H. Karmaker, R. Badcock, B. Buckley, T. Haugan, M. Izumi, D. Loder, J. W. Bray, P. Masson, and E. W. Stautner, High power density superconducting rotating machines—development

status and technology roadmap, Supercond. Sci. Technol. **30**, 123002 (2017).
[24] C. Hoffmann, R. Walsh, E. Karrer-Mueller, and D. Pooke, Design parameters for an HTS flux pump, Phys. Proc. **36**, 1324 (2012).
[25] R. M. Walsh, R. Slade, D. Pooke, and C. Hoffmann, Characterization of current stability in an HTS NMR system energized by an HTS flux pump, IEEE Trans. Appl. Supercond. **24**, 4600805 (2014).
[26] S. L. Wipf, in *Proceedings of the 1968 Summer Study On Superconducting Devices and Accelerators* (Brookhaven, New York, United States, 1968), p. 632.
[27] O. Mawardi, A. Gattozzi, and H. Chung, Operational characteristics of a flux pump, IEEE Trans. Magn. **15**, 828 (1979).
[28] S. Kalsi, *Applications of High Temperature Superconductors to Electric Power Equipment* (Wiley-Blackwell, Hoboken NJ, USA, 2011), Chap. 3, p. 35.
[29] H. W. Weijers, W. D. Markiewicz, A. J. Voran, S. R. Gundlach, W. R. Sheppard, B. Jarvis, Z. L. Johnson, P. D. Noyes, J. Lu, H. Kandel, H. Bai, A. V. Gavrilin, Y. L. Viouchkov, D. C. Larbalestier, and D. V. Abraimov, Progress in the development of a superconducting 32 T magnet with REBCO high field coils, IEEE Trans. Appl. Supercond. **24**, 4301805 (2014).
[30] D. X. Ma, S. Matsumoto, R. Teranishi, T. Ohmura, T. Kiyoshi, A. Otsuka, M. Hamada, H. Maeda, Y. Yanagisawa, H. Nakagome, and H. Suematsu, Degradation analysis of REBCO coils, Supercond. Sci. Technol. **27**, 085014 (2014).
[31] J. Ma, J. Geng, J. Gawith, H. Zhang, C. Li, B. Shen, Q. Dong, J. Yang, J. Chen, Z. Li, and T. A. Coombs, Rotating permanent magnets based flux pump for HTS no-insulation coil, IEEE Trans. Appl. Supercond. **29**, 8663420 (2019).
[32] J. Geng and M. Zhang, A parallel co-wound no-insulation REBCO pancake coil for improving charging delays, Supercond. Sci. Technol. **32**, 084002 (2019).
[33] M. Faraday, Experimental researches in electricity, Phil. Trans. R. Soc. London **122**, 125 (1832).
[34] W. Wang and T. Coombs, Macroscopic Magnetic Coupling Effect: The Physical Origination of a High-Temperature Superconducting Flux Pump, Phys. Rev. Appl. **9**, 044022 (2018).
[35] K. Kajikawa, T. Hayashi, R. Yoshida, M. Iwakuma, and K. Funaki, Numerical evaluation of AC losses in HTS wires with 2D FEM formulated by self magnetic field, IEEE Trans. Appl. Supercond. **13**, 3630 (2003).
[36] Z. Hong, A. M. Campbell, and T. A. Coombs, Numerical solution of critical state in superconductivity by finite element software, Supercond. Sci. Technol. **19**, 1246 (2006).
[37] R. Brambilla, F. Grilli, and L. Martini, Development of an edge-element model for AC loss computation of high-temperature superconductors, Supercond. Sci. Technol. **20**, 16 (2006).
[38] M. D. Ainslie, T. J. Flack, and A. M. Campbell, Calculating transport AC losses in stacks of high temperature superconductor coated conductors with magnetic substrates using FEM, Phys. C **472**, 50 (2012).
[39] M. D. Ainslie, C. W. Bumby, Z. Jiang, R. Toyomoto, and N. Amemiya, Numerical modelling of dynamic resistance in high-temperature superconducting coated-conductor wires, Supercond. Sci. Technol. **31**, 074003 (2018).
[40] R. A. Badcock, S. Phang, A. E. Pantoja, Z. Jiang, J. G. Storey, H. Sung, M. Park, and C. W. Bumby, Impact of magnet geometry on output of a dynamo-type HTS flux pump, IEEE Trans. Appl. Supercond. **27**, 5200905 (2017).
[41] A. E. Pantoja, Z. Jiang, R. A. Badcock, and C. W. Bumby, Impact of stator wire width on output of a dynamo-type HTS flux pump, IEEE Trans. Appl. Supercond. **26**, 1 (2016).
[42] J. R. Clem, Theory of flux-flow noise voltage in superconductors, Phys. Rev. B **1**, 2140 (1970).
[43] E. H. Brandt and M. Indenbom, Type-II-superconductor strip with current in a perpendicular magnetic field, Phys. Rev. B **48**, 12893 (1993).
[44] V. M. R. Zermeño, A. B. Abrahamsen, N. Mijatovic, B. B. Jensen, and M. P. Sørensen, Calculation of alternating current losses in stacks and coils made of second generation high temperature superconducting tapes for large scale applications, J. Appl. Phys. **114**, 173901 (2013).
[45] C. Plummer and J. Evetts, Dependence of the shape of the resistive transition on composite inhomogeneity in multifilamentary wires, IEEE Trans. Magn. **23**, 1179 (1987).
[46] J. Rhyner, Magnetic properties and AC-losses of superconductors with power law current–voltage characteristics, Phys. C **212**, 292 (1993).
[47] N. M. Strickland, C. Hoffmann, and S. C. Wimbush, A1 kA-class cryogen-free critical current characterization system for superconducting coated conductors, Rev. Sci. Instr. **85**, 113907 (2014).
[48] S. C. Wimbush and N. M. Strickland, A public database of high-temperature superconductor critical current data, IEEE Trans. Appl. Supercond. **27**, 8000105 (2017).
[49] F. Grilli, A. Morandi, F. D. Silvestri, and R. Brambilla, Dynamic modeling of levitation of a superconducting bulk by coupled H-magnetic field and arbitrary lagrangian—eulerian formulations, Supercond. Sci. Technol. **31**, 125003 (2018).
[50] L. Quéval, K. Liu, W. Yang, V. M. R. Zerme no, and G. Ma, Superconducting magnetic bearings simulation using an H-formulation finite element model, Supercond. Sci. Technol. **31**, 084001 (2018).
[51] V. V. Andrianov, V. B. Zenkevich, V. V. Kurguzov, V. V. Sychev, and F. F. Ternovskiĭ, Effective resistance of an imperfect type II superconductor in an oscillating magnetic field, Soviet J. Exp. Theor. Phys. **31**, 815 (1970).
[52] J. M. Brooks, M. D. Ainslie, Z. Jiang, A. E. Pantoja, R. A. Badcock, and C. W. Bumby, The transient voltage response of ReBCO coated conductors exhibiting dynamic resistance, Supercond. Sci. Technol. **33**, 035007 (2020).
[53] J. Volger and P. Admiraal, A dynamo for generating a persistent current in a superconducting circuit, Phys. Lett. **2**, 257 (1962).
[54] O. Mawardi and S. Xu, Armature reaction in a flux pump, IEEE Trans. Magn. **23**, 587 (1987).
[55] R. Mataira, M. D. Ainslie, R. Badcock, and C. W. Bumby, Modeling of stator versus magnet width effects in high-T_c superconducting dynamos, IEEE Trans. Appl. Supercond. **30**, 5204406 (2020).